The Journal of the Acoustical Society of America

JUNE 18 2026

Temporally stable bottom-interacting upslope sound propagation south of Malta

Timothy F. Duda ; Pierre-Marie Poulain ; Silvia Falchetti; Giuliana Pennucci ; Paolo Oddo ; Giacomo Giorli

J. Acoust. Soc. Am. 159, 5476–5490 (2026)
https://doi.org/10.1121/10.0043949

JASA ARTICLE

Temporally stable bottom-interacting upslope sound propagation south of Malta

Timothy F. Duda,[1,a)] Pierre-Marie Poulain,[2] Silvia Falchetti,[3] Giuliana Pennucci,[3] Paolo Oddo,[4] and Giacomo Giorli[3]
[1]Applied Ocean Physics and Engineering Department, Woods Hole Oceanographic Institution, Woods Hole, Massachusetts 02543, USA
[2]Istituto Nazionale di Oceanografia e di Geofisica Sperimentale, Sgonico (Trieste), Italy
[3]NATO-STO-CMRE, La Spezia 19126, Italy
[4]Department of Physics and Astronomy, University of Bologna, Bologna 40126, Italy

ABSTRACT:
The influence of dynamical ocean features on seabed-interacting acoustic transmissions was investigated southeast of Malta in the Mediterranean Sea. Waveforms at 610–890 Hz were transmitted to mimic impulse propagation over two fixed paths of 25 and 45 km length. Area conditions included topographically trapped diurnal waves, stochastic internal waves, a 60-m-thick surface mixed layer, and weak mesoscale flows. Many stable arrivals with transmission loss of 57 to 66 dB were observed on the short path. The matched-filter recovered impulse response showed a high degree of temporal coherence over the 5-d-long experiment. Travel times of tracked individual signal peaks showed root mean square variation of 3 ms. Much of this reported travel-time variability results from slowly fluctuating dominance between micromultipaths, rather than time variation of a single steady ray. Spectral analysis of the travel times provided weak evidence of a peak at the diurnal tidal frequency, with no reliable evidence of semidiurnal-band oscillations of arrival peak levels or times. Most rays interact with the seabed, and model simulations with different bottom attenuation coefficients support intuition that seabed properties determine a base-state transmission loss and impulse response in the area, only slightly modified by water column variations.
 https://doi.org/10.1121/10.0043949

(Received 12 February 2026; revised 8 May 2026; accepted 12 May 2026; published online 18 June 2026)
[Editor: Kay L. Gemba] Pages: 5476–5490

I. INTRODUCTION

Seabed-interacting sound propagating upslope in the ocean often displays strong time variability caused by many environmental factors (Duda *et al.*, 2004; Sperry *et al.*, 2003; Chiu *et al.*, 2004; DeCourcy *et al.*, 2022; Johnson *et al.*, 2023). Underwater sound is always affected by sound-speed variability in the water itself. Additionally, when sound moves upslope and encounters the seabed, rays are deflected to steeper angles upon reflection, increasing the rate of surface and seabed interaction as distance grows. This can amplify the effects of water column sound-speed variations because altered rays interact with the boundaries at new (and possibly more) locations, potentially changing all aspects of the reflection process. In this work, 610–890 Hz linear frequency modulated (LFM) pulses propagating 25 and 45 km from a deep-water source to shallow-water receivers on the south side of the Malta Plateau in the central Mediterranean Sea are analyzed, and the stability of seabed interacting sound is quantified. The arriving sound was more stable in this study than sound in some recent experiments (e.g., Johnson *et al.*, 2023, their Fig. 2). Some of those experiments were conducted in dynamically active areas, thus not contributing to knowledge of conditions in less energetic areas (Duda *et al.*, 2004; Sperry *et al.*, 2003; Chiu *et al.*, 2004). The study reported here used matched-filtering pulse synthesis with higher bandwidth than was used in some previous upslope studies at 200 to 500 Hz (Duda *et al.*, 2004; Sperry *et al.*, 2003; Chiu *et al.*, 2004), allowing better multipath resolution. Johnson *et al.* (2023) and Decourcy *et al.* (2022) used 400-Hz bandwidth sources centered at 725 Hz to study upslope propagation, similar to this study. An interesting aspect of this study is that tidal-frequency sound-speed perturbations compose a large fraction of the total sound-speed variability, whereas the received sound variability is spread over a wide swath of frequencies. This implies that macroscopic sound pathways are unaffected by the tidal sound-speed anomalies, and that time-dependent splitting of sound rays into microrays and resultant micromultipath interference plays an important role in the time-dependence of the propagation (DeFilippis *et al.*, 2023). This paper analyzes a set of stable ray-like arrivals along the two paths and interprets the behavior in terms of surface reflection variability and microray interference.

Data from the study area showed sound-speed variability dominated by boundary-trapped internal tides (ITs), with

[a)]Email: tduda@whoi.edu

other internal waves contributing. ITs (internal waves at tidal frequency), are an important source of sound-speed anomalies at many locations, with examples discussed in the next paragraph. ITs can be either primary or secondary causes of acoustic propagation time dependence, depending on the relative strengths of the sound-speed anomalies they cause and any other time-dependent anomalies. Although ITs have been observed since the early 20th century (Nansen, 1902; Petterson, 1907), their direct measurements became possible only in more recent times with the advancements in the technology of oceanographic instruments (Wunsch, 1975). ITs are generated by the interaction of barotropic tidal currents (currents from surface tides) with the topography of the ocean floor (Morozov, 2006; St. Laurent *et al.*, 2003; Merrifield *et al.*, 2001), and they have a profound role in the general mixing in the ocean (St. Laurent and Garrett, 2002) as well as in the dissipation of tidal energy (Munk and Wunsch, 1998). We find that ITs have a small effect on sound at the Malta site, which contrasts with their measurable effects noted in other studies, referred to in the paragraphs to follow.

The Malta Plateau study area has relatively strong ITs with respect to internal waves of other frequencies (Poulain *et al*. 2023). As they propagate in an area, internal waves and ITs generate oscillations of the isotherms, isopycnals, and isohalines in the water column, thus altering the sound velocity field (Robertson and Hartlipp, 2014; Tiemann *et al.*, 2001; Colosi *et al.*, 2013; Chiu *et al.*, 2004). In some areas, such as the Philippine Sea, vertical displacement of isopycnals and isotherms at tidal frequencies dominates the sound-speed variability (Colosi *et al.*, 2013). Non-tidal internal waves, subtidal effects, and barotropic tides also affect the sound-speed field, acoustic propagation paths, and acoustic travel times.

In the past, absolute acoustic travel times were measured in the Strait of Gibraltar, and the travel times of early arrivals, in a multipath setting, showed a tidal signal (Tiemann *et al.*, 2001). In another study conducted in the South China Sea, ITs and solitons influenced the received levels of phase-modulated signals with a carrier frequency of 400 Hz (Chiu *et al.*, 2004; Duda *et al*. 2004). This paper describes a situation not covered by those works, 25 and 45 km upslope propagation paths with center frequency and bandwidth high enough to resolve ray arrivals, and to make vertical modal arrivals too complex to be understandable without a dense array receiver. Interestingly, although ITs are a primary component of sound-speed variability observed in the area, IT effects on sound are minimal. Instead, other factors control the macroscopic nature of the sound propagation, which is stable for the 5 days of the experiment, and control the ray splitting into microrays from either turning-point effects (Duda and Bowlin, 1994; DeFilippis *et al.*, 2023) or reflection effects.

The paper is organized as follows. Section II describes the experiment area and methods. Section III presents the acoustic data, some simulation results, and compares these two. Section IV discusses the results and presents some interpretation. Section V is a summary.

II. EXPERIMENT AREA AND METHODS

A. Geography and experiment layout

The experiment was carried out southeast of Malta in the Sicily Channel of the central Mediterranean Sea (Fig. 1). This was part of the Mediterranean Recognized Environmental Picture (2020) (MREP20) sea trial conducted by NATO Science and Technology Organization Centre for Maritime Research and Experimentation (CMRE). The scope of the trial was to study the oceanographic and acoustical properties of frontal zones where the Eastern and Western Mediterranean water converge. The MREP20 temperature, salinity, and current data evidenced variability at the mesoscales and submesoscales that included a weak frontal system that separates the Atlantic fresher waters from the Ionian saltier waters (Oddo *et al.*, 2023). Three acoustic moorings were situated such that the source (Tx) was at the south in the deepest water, and two receivers (Rx2 and Rx3) were at the north at distances from Tx of 25 km (Rx2) and 45 km (Rx3) (Fig. 1). A fourth mooring collected physical oceanographic data (W1). The seabed along the short path was slightly upslope (Fig. 1). The seabed along the longer path was slightly upslope than more steeply upslope to the outer-shelf receiver (Fig. 1). As will be shown, at the time of operations, a bottom-focused diurnal tidal oscillation dominated the sound-speed variability (Poulain *et al.*, 2023), but the acoustic fluctuations were not primarily diurnal. The environmental regimen of stratification and tidal oscillations may be unique to this site.

B. Circulation and stratification

In the eastern Sicily Channel, in the central Mediterranean Sea, there is a net eastward flow of Atlantic Water at the surface, and there are eddies generated by topographic features and internal baroclinic effects. A deeper layer of Levantine Intermediate Water flows to the west, and it is mainly constrained by the bottom topography (Lermusiaux and Robinson, 2001; Astraldi *et al.*, 1996, 1999, 2002; Lermusiaux, 1999; Millot, 1987; Béranger *et al.*, 2004).

C. Surface tides and ITs

Tides in the Mediterranean Sea have smaller amplitudes than ocean tides. However, in some areas, the tidal currents can reach considerable speeds. In addition to the locally generated tides, Atlantic tides propagate into the sub-basins of the Mediterranean Sea (Lozano and Candela, 1995; Tsimplis *et al.*, 1995). In the studied area, the primary tidal sea level variations are those of the M2 semidiurnal constituent (Grancini and Michelato, 1987), while the tidal currents are dominated by the K1 constituent (Cosoli *et al.*, 2015; Poulain *et al.*, 2018). Studies have shown that this diurnal current amplification happens in the eastern Alboran Sea, Sicily Channel, and northern Adriatic Sea (Poulain *et al.*, 2018). This effect has been reported on the Sicilian continental shelf, with diurnal oscillations around Malta

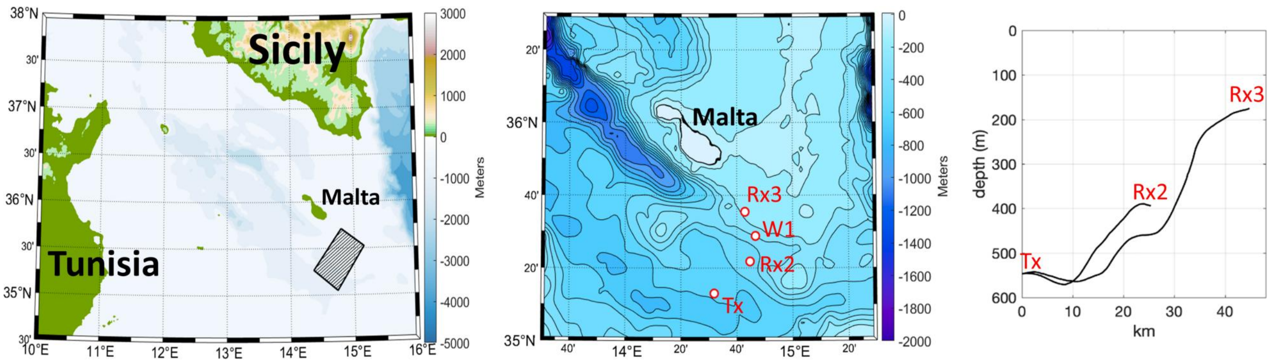

FIG. 1. Study area (left, black box) of the MRE20 sea trial and a zoomed map (middle) indicating the location of the moorings Tx, Rx2, Rx3, and W1 used in this study. Sicily is north of the study area and Tunisia to the West (left). The bathymetric profiles (right) from the European Marine Observation and Data Network (EMODnet), used for sound simulations, are shown for the two acoustic paths.

(Tsimplis *et al.*, 1995), and to the east on the Maltese Bank (Grancini and Michelato, 1987; Poulain *et al.*, 2018).

Analysis of the MREP20 dataset revealed that strong diurnal baroclinic tidal displacements existed on the Maltese Bank. Mixed diurnal and semidiurnal internal tidal signals were found in the deeper water to the south. The measurements also evidenced that tidal currents are dominated by a diurnal constituent (K1) that is not accompanied by a dominant diurnal tidal elevation signal. The sea-level signal is mainly an M2 semi-diurnal oscillation. Poulain *et al.* (2023) reported that the K1 component propagates as a Kelvin-type bottom trapped wave northwestward with an estimated phase velocity of 1 m/s and a wavelength of ∼100 km, but the study could not disclose where these ITs are generated. In a follow-up study (Oddo *et al.*, 2023), ITs at the Maltese Banks have been further investigated and modeled using the oceanographic dataset collected during the same experiment (MREP20). The work further demonstrated that the baroclinic variability in the area was indeed dominated by diurnal ITs, and discovered that they are generated by the interaction of the barotropic tidal flows with the steep bathymetric gradient between the Sicily Channel and the Ionian Sea.

D. Measurement methods and data types

MREP20 took place between October 27 and November 8, 2020, with the acoustic measurements described here taken November 1–6. Using NRV *Alliance*, CMRE deployed, among many other assets, a mooring with oceanographic sensors and a sound source (Tx), two moorings with hydrophones and oceanographic sensors (Rx2 and Rx3), and a mooring denoted W1 carrying a WireWalker profiler (Del Mar Oceanographic, San Diego) (Fig. 1). A complete description of the sea trial methodology is reported in Poulain *et al.* (2023) and Oddo *et al.* (2023). The Tx, Rx2, and Rx3 moorings were equipped with several oceanographic sensors to measure conductivity, temperature, and pressure [built by Sea-Bird Electronics (SBE, now Sea-Bird Scientific, Bellevue, WA), RBR (Canada), and Star-Oddi (Iceland)]. In this study, we use the sound emitted from Tx and received at Rx2 and Rx3 (Fig. 1). Oceanographic data from the moorings are also used.

Mooring Tx carried a sound source designed by the Woods Hole Oceanographic Institution (WHOI). The source was placed 130 m below the sea surface. An IcListen hydrophone (Ocean Sonics, Truro Heights, Nova Scotia, Canada) was also mounted on Tx, 50 m below the source, continuously sampling at 50 kHz. The source transmitted 5-second-long LFM sweeps (610–890 Hz) that were intended to be emitted twice every 20 s between the 5th and the 25th minute, and the 35th and 55th minute of each hour. Up and down-sweeps were alternated, and only the upsweeps at 20-s repeat rate are analyzed here. However, hardware and firmware performance issues created a silent gap of a few minutes during most of the 20-min transmission windows. This does not impact the results, but it does reduce the number of pulses used to compute statistical quantities. The transmissions started at the beginning of November 1. The Tx hydrophone was used to measure the transmission times and levels of each LFM emitted by the source.

Mooring Rx2 had two WHOI Several Hydrophone Receiver Units (SHRUs), each one equipped with four hydrophones sampled at 9765.625 Hz. Hydrophone depths were 65, 85, 105, and 125 m for the upper unit, and 145, 165, 185, and 205 m for the lower unit. Temperature was measured at 13 levels, while conductivity was measured at three of the levels yielding salinity. The flow-induced horizontal displacement time-series of the Rx2 receivers is not corrected for in this study. The Rx2 sound receptions shown throughout this paper are obtained by matched-filter processing the receptions via cross correlation with the waveform. A normalization is applied so that the matched-filter peak height is equal to an arriving multipath signal root mean square (RMS) sound pressure level. Filtering to remove sound at frequencies below and above the signal band of 610–890 Hz was not done because of the high signal-to-noise ratio (SNR) of the main signals, and filter choice would be subjective. Thus, ambient sound at all recorded frequencies contributed to the matched-filtered waveform time series.

The Rx3 mooring was equipped with an 8-channel linear vertical array (SLIVA) recording continuously at a sampling rate of 50 kHz. The eight hydrophones spanned a length of 50 m and the center of the array was at about 90 m of depth. Two SBE pressure sensors on the Tx mooring and two RBR pressure sensors on the Rx3 mooring were used to evaluate effects of mooring lateral motions by estimating the mooring slant angle (α) and the horizontal displacement (dx) of the Tx source and the SLIVA using the following equations:

$$\alpha = \cos^{-1}\frac{(S_2 - S_1)}{D}, \tag{1}$$

$$dx = (B - Z) \times \sin\alpha, \tag{2}$$

where S_2 and S_1 are the depths measured by the deeper and shallower depth sensor, respectively; D is the nominal distance between the sensors; B is the depth of the bottom of the ocean; and Z is the unperturbed depth of the element to be localized (Tx source and the SLIVA array). SBEs were deployed at 107 and 162 m on Tx; RBRs at 36 and 153 m were used on Rx3. With this approach, we could not determine the direction of the swinging movement of the moorings; nevertheless, these estimates were used to compute upper bounds for travel time alterations caused by mooring displacement.

The main instrument at W1 was an RBR Concerto conductivity-temperature-depth device sampling at 8 Hz, used to measure the velocity of sound as a function of time and depth. As explained by Poulain *et al.* (2023), all the W1 upcasts consistently lasted about 5 min, while the W1 downcasts had a high variability in their descent rates. Hence, only W1 upcasts data were used.

The transmissions from Tx were recorded at Rx2 from 00:05 UTC on November 1 to 06:17 UTC on November 6, 2020 when Rx2 was recovered, and at Rx3 until the end of November 6. Figure 2 shows matched-filter output for Rx2 recordings at the 85-m depth hydrophone. The time series at the other hydrophones had similar qualities and are not examined here. The figure shows a reduced set of arrivals, one pulse each 15 min. The time shown (t_r) is relative to a distance-determined mean travel time (t_{tt}) and time trend that offsets a steady drift (t_d) in the sound source time base, $t_r(t) = t - t_{tt} - t_d(t)$. The SNR of the highest peak is often over 50 dB and typically over 35 dB. The impulse response lasts approximately 0.8 s. There are some steady but weak early arrivals, a strong arrival, a pair of strong arrivals, two intervals with fluctuating arrivals, and finally two weak fluctuating arrival intervals. On the right, Fig. 2(b) shows the strong arrivals. This Rx2 impulse response, and a similar impulse response recorded at Rx3, will be analyzed further in Sec. III.

The W1 profiler produced a time series of temperature T and salinity S versus pressure (depth) and time, $T(P,t)$ and $S(P,t)$. Figure 3 shows the W1 data and two sound-speed profiles from W1. A very strong thermocline/pycnocline is evident, shoaling from about 75 to about 60 m in the record. Quantifying the local internal tidal signals, Poulain *et al.* (2023) reported the diurnal oscillations to be typically 15–25 m in height at around 160 m depth, with vertical velocities of 0.1–0.2 m/s, and that semidiurnal oscillations with a local maximum at 170 m were present but of much smaller amplitude. Local maxima for the K1 and M2 ITs were also measured at the base of the mixed layer. In general, their harmonic analysis tidal model (K1 + M2) explained 60%–80% of the total variability.

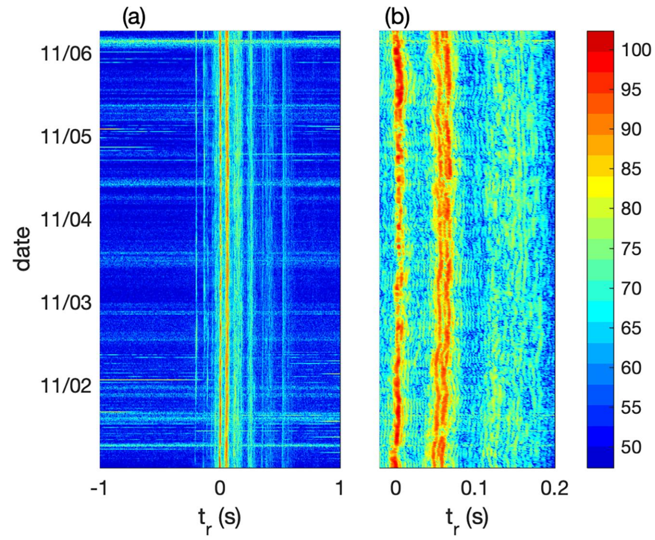

FIG. 2. (a) The impulse response recorded in dB re 1 micropascal at the 85-m depth Rx2 phone. A decimated set of the full set of impulses is shown here, with a 15-min sample rate, four pulses per hour. (b) An expanded view of the time window with two strong peaks and the first interval of fluctuating arrivals. We refer to these features as Arrival 1 (arr 1, usually a single peak) at time zero in the plot, Arrival 2 (usually a pair of peaks), and Arrival 3 (the interval after 0.1 s).

E. Acoustic analysis methods for Rx3 arrivals

The receptions at Rx2 were processed in a routine way, with a clock drift fitted after the data were matched-filtered. Rx3 hydrophone data were matched-filter processed in the same way, but an automated method was used to extract multipath arrivals (pick peaks) in the filtered dataset. The transmission, reception, and travel times were measured by matched-filtering the recorded signal on the IcListen mounted on the Tx mooring and the signal recorded by channel 4 (about 80 m of depth) of the SLIVA array on the Rx3 mooring with a synthetic replica of the real LFM waveform. All times for transmissions and receptions were measured from the sample numbers. Time zero was the first acoustic pressure measurement recorded by the IcListen for the transmissions and by the SLIVA for the receptions. The method was adopted to mitigate the effects of interfering acoustic signals at Rx3.

The source and the SLIVA array clocks were not synchronized and drifted at different rates. To identify each pair of transmission/detection, we adopted a pattern analysis approach based on the relative time of the first transmission. The pattern of transmissions detected on IcListen at Tx should match the pattern of receptions detected on the SLIVA at Rx3. This way, the Tx and SLIVA clock offsets could be disregarded, and Tx transmission gaps served as timing

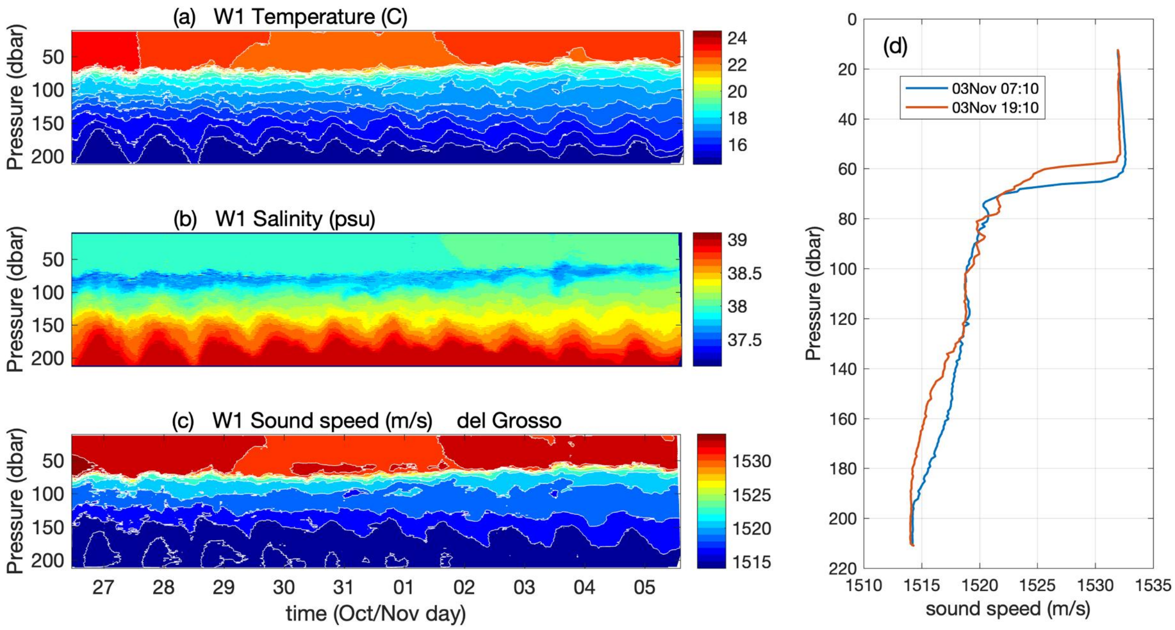

FIG. 3. (a) Temperature at W1. See (c) for time axis label. (b) Salinity at W1. (c) Sound speed at W1. The time axis is labeled such that November 1 begins at time label 01. (d) Two W1 sound-speed profiles. One profile (red line, lower value at 160-m depth) was taken when the deep isotherm oscillation was at a peak in height (19:10 November 3), the other profile (blue line) 12 h earlier in the trough. Large diurnal water column oscillations are seen deeper than 125 m. Spring tide peak is October 31.

identifiers. For this pattern analysis, we first matched the transmission times with the times of arrival at Rx3 of the strongest arrivals. Once each transmission was matched with a dominant arrival at Rx3, we then associated each multipath arrival within 0.6 s to its respective transmission. The 0.6-s time window for this analysis was used after inspecting the matched-filter outputs. We observed that a 0.6 s time window was long enough to capture the multipath arrivals.

The received levels of each multipath arrival at the SLIVA were computed in dB from their corresponding peak of matched-filter output. The travel time between each transmission and its respective reception (including multipath arrivals) was then computed relative to the travel time of the first reception of the study. The one-way travel time set was detrended by removing the best straight-fit line from the data to remove the effects of the clock drifts. Figure 4 shows the multipath arrivals, both with and without detrending. This pattern analysis generated a dataset of 12 133 matched pairs of transmission/receptions and 70 349 multipath receptions. For comparison, 120 upsweeps/h for 5.2 days is 14 976. Some very persistent arrivals with strong intensity variations are evident, along with some intermittently detected arrivals.

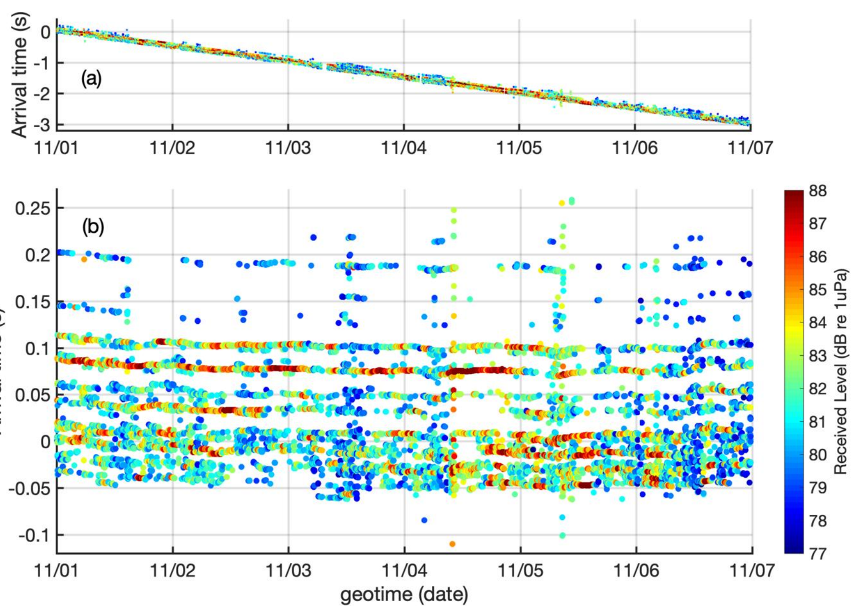

FIG. 4. (a) Identified Rx3 matched-filter phone-4 peaks. (b) The identified Rx3 matched-filtered peaks after accounting for uniform clock drift.

https://doi.org/10.1121/10.0043949

The procedure provides a picture with less dynamic range of intensity than the conventional Rx2 processing, but sufficiently shows the behavior of the strongest arrivals.

III. ACOUSTIC DATA AND COMPARISON TO SIMULATIONS

A. Rx2 observed arrivals

The multipath arrival structure of sound at Rx2 (Fig. 2) begins with four weak intermittent arrivals that are followed by one strong arrival and a pair of strong arrivals. After that are four bands of fluctuating weak sound. This is shown in Fig. 5. The figure shows a mean pulse produced by oversampling each matched-filtered waveform to yield a 48-kHz sample rate, then detrending to remove clock drift, then time averaging. The mean first strong arrival is narrow despite some small arrival time wander, whereas the second strong arrival is widened and averaging the wander causes the two peaks to essentially merge. The four peaks (p annotation in Fig. 5) that precede the strong arrivals (arr 1, arr 2) are steady in form and appear narrow, even after averaging over 5 days. Conversely, the groups of arrivals (lines g) that follow the strong arrivals are spaced closely together and fluctuate in time such that 5-day mean does not show narrow peaks. The figure also shows moderately well-fitting simulated pulse snapshots (see Sec. III E).

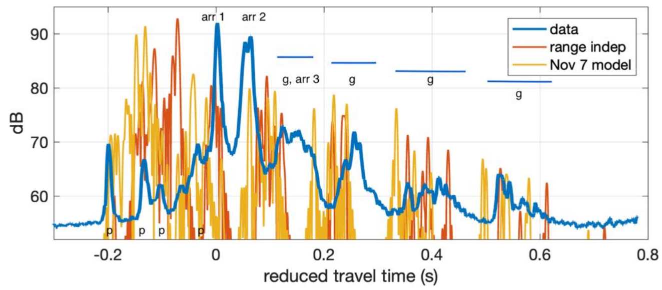

FIG. 5. The thick blue line indicates time-mean of the detrended 15-min subsampled Rx2 arrivals of Fig. 3. Each arrival is oversampled before the averaging is done. Four narrow (steady in time) weak arrivals before the three strong main arrivals are visible, marked "p." After the 90-dB main arrivals, four wide time-windows marked "g" filled with fluctuating sound sum to low levels no higher than 73 dB, 20 dB below the main peak. Two BELLHOP3D modeled pulse arrival snapshots (not averages) are also shown. One is for a range-independent sound speed situation, and the other is for 3D-variable sound-speed from a data-assimilating model.

B. Rx2 arrival short-term stability

The arriving multipath signals have high temporal coherence at short time intervals, i.e., are very stable in form. This is not evident in Fig. 2 because only one pulse every 15 min is shown over the many-day period. Figure 6 shows high rep-rate data for the two strong arrivals (arr 1 and arr 2) and the first diffuse arrival (arr 3) for four 20-min pulse groups, called geotimes 1–4. Shown are color plots of matched-filter output (micropascals) in pulse-time/clocktime format, and time-mean pulses for the 20-min windows. The first examined 20-min period (geotime 1) has intermittent noise that is near the highest observed level, with noise levels in the matched-filter time series varying from the typically observed low level of 50 to 82 dB. Geotimes 2 and 3 are consecutive, with geotime 2 showing a transition of the first arrival to a new time (new path) as an arrival fades. Geotime 4 shows sound that is steady at a time of typically low noise.

The stability of arrivals at Rx2 can be quantified with correlation (cross correlation) functions computed for pairs of waveform profiles separated in time. Figure 7(a) shows correlation functions for time separations of up to 20 min. Twelve are shown, covering arr 1, arr 2, and arr 3 over the four geotime windows. These are computed by first forming the pair-wise cross-product (inner product) of waveforms separated in time [clock time t with lag (separation) τ], and also lagged by time within the pulse waveform (also called fast time t_f, with $t_1 < t_f < t_2$, and with lag δt_f), then taking the maximum with respect to fast time lag. Before the maximum-taking step, the inner products are normalized such that autocorrelations at zero lag equal to 1. The expression for the temporal correlation function for a collection of time-lagged matched-filtered waveforms Φ is as follows:

$$R(\tau) = \left\langle \max_{\delta t_f} \left\{ \frac{\sum_{t_f=t1}^{t2} \Phi(t_f, t)\Phi(t_f + \delta t_f, t + \tau)}{\left(\sum_{t_f=t1}^{t2} \Phi^2(t_f, t)\right)^{1/2} \left(\sum_{t_f=t1}^{t2} \Phi^2(t_f, t + \tau)\right)^{1/2}} \right\} \right\rangle, \quad (3)$$

where t_f indicates time incremented within the waveform. The angle brackets indicate ensemble average over correlations of pairs of pulses sharing a common lag τ. This procedure is like that used by Duda *et al.* (2012) to compute coherency of broadband waveforms. In that paper, spatially lagged correlation along an array was computed, with the maximum-taking step used to accommodate along-array arrival time delay, also called arrival time wander

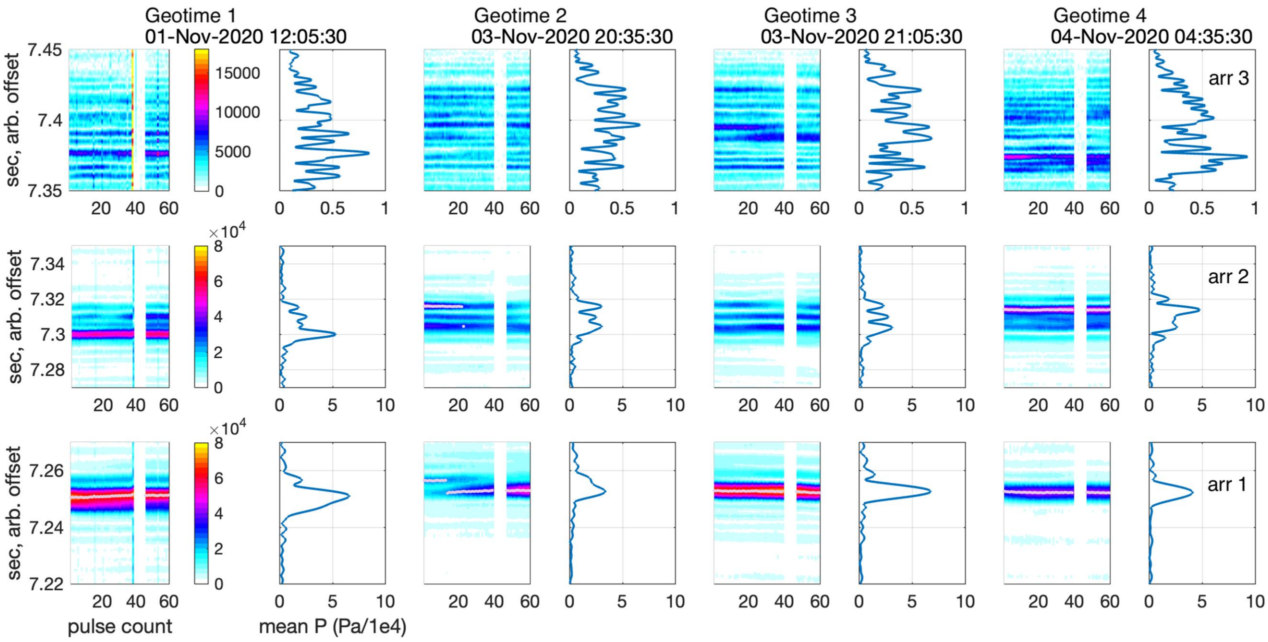

FIG. 6. The matched-filtered Rx2 signals of the two strong peaks and the interval of fluctuating arrivals are shown for four 20-min pulse windows. These windows are named geotimes 1–4 as labeled. Three arriving waveform sections are depicted bottom to top: (bottom row) arr 1 first strong arrival; (middle row); (top row) arr 3 weak arrival period, signals 20 dB below arr 1. The "fast time" pulse arrival time axis has an arbitrary offset that differs from the offset in Figs. 2, 4, and 5. For each geotime, the pulse groups and the time-mean pulse are shown in left/right pairs, with the time-mean pulse (micropascals) on the right, and the 60 repeats of the arriving sound (3 per minute) on the left. Geotime 1 is a period with elevated noise. Geotimes 2 and 3 are two consecutive 20-min windows that show some pulse transitions that exceed what was typically observed. Geotime 4 has low noise and a typically steady first arrival at 7.25 s.

(Flatté *et al.*, 1979). Here, using the maximum, which may not be at fast time lag 0, also accommodates wander that does not effect waveform shape. The use of the matched-filter processed waveforms mitigates the effects of noise on the estimated signal coherence. However, some brief instances of high noise and the steady moderate noise, as shown in for arr 3 at geotime 1 in Fig. 6, do alter the temporal coherence structure, so the mitigation is not complete and the computed R values are lower bounds. The R values are above 0.9 except for the 7.22–7.27 s (first arrival) time window with the multipath transition, geotime 2. Figure 7(b) shows the R functions for the entire received waveform, which has properties similar to the short time-window functions of Fig. 7(a). Geotime 1 has a noise event that distorts the function. Geotime 2 has a micromultipath transition that reduces correlation. The other two 20-m windows (geotimes) show high R. For comparison, the ASIAEX 2001 dataset from a shelf-edge environment with energetic ITs

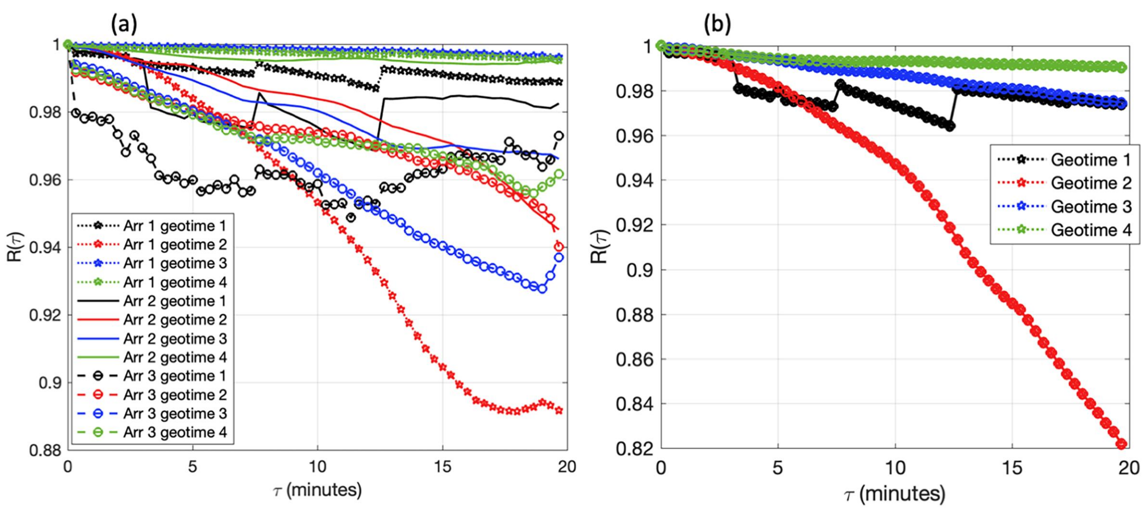

FIG. 7. (a) The time-lagged maximum normalized correlation of each of the 12 multipath sequences shown in Fig. 6 (three steady arrivals, four geotimes). The geotime 1 sound (plotted in black) has lower SNR. The immediate drop for arrival 3 geotime 1, and the fluctuations at 4, 8, and 12 min for the other geotime arrivals, are caused by incoherent noise. Geotime 2 sound has a multipath transition and a reduced correlation. Geotime 4 sound has high temporal correlation that is typical for the experiment. (b) Correlation calculated for the entire waveform, 7.2–7.5 s reduced time.

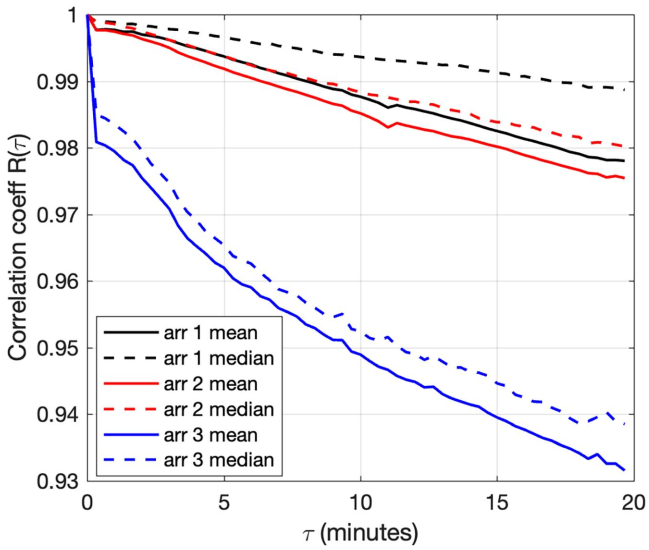

FIG. 8. The time-lagged correlation functions calculated by averaging over the entire 5-d series of pulses recorded at Rx2 are shown with solid lines. These are the means of the R values obtained by averaging within 20-min pulse windows. The median over the record of the individual 20-min R estimates is given by the dashed lines.

and nonlinear waves showed e-folding correlation times of 2–15 min for snapshots of vertically sampled narrowband signals extracted from broadband signals (Mignerey and Orr, 2004).

Figure 8 shows the mean $R(\tau)$ functions for the three analyzed arrival groups (two strong arrivals, arr1 and arr2, and the first extended arrival group, arr3) computed for all pulses over the 5 day experiment. These curves corroborate the finding understood from the careful examination of the selected pulses analyzed in Figs. 6 and 7. The 5-d median values are higher than the mean correlation coefficient values, showing that outlier events reduce the mean. Reduced R is associated with noise events, such as those examined in Figs. 6 and 7.

C. Rx2 arrival long-term tidal periodicity and stability

The signal correlation at time lags longer than 20 min is examined using ensemble averages of the matched-filter arrival time series in each 20-min window, which we refer to as the mean pulses for the 20-min windows. Figure 6 shows portions of the mean pulses for four geotimes as line plots. Two parameters are used to quantify window-mean peaks that are sustained in the 6-day time series: the travel-time anomaly of a given peak (arrival time of a persistent peak after clock corrections with the mean corrected time removed), and the peak level. Figure 9 shows these parameters for the first strong arrival (at time zero in Figs. 2 and 5 and time 7.25 in Fig. 6). The peak level [Fig. 9(a)] varies over 20 dB, with an RMS fluctuation of 4.6 dB. The time anomaly range is about 12 ms [Fig. 9(b)]. Figure 9(c) shows the spectrum of the time variations computed using eigenvalue spectrum and periodogram methods. The eigenvector method (Marple, 1987), suitable for analyzing sums of sinusoids, produces parameter-dependent results. The method computes eigenvalues and eigenvectors of the autocorrelation function, with parameter p being the number of

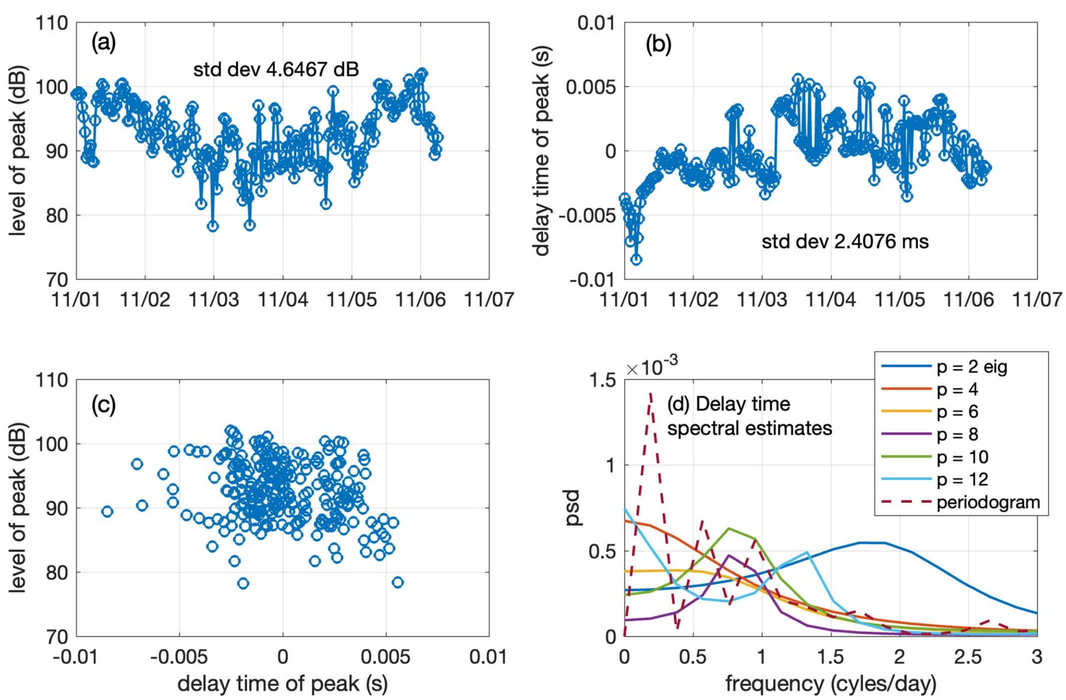

FIG. 9. (a) The time series of peak matched-filtered sound intensity for the first main arrival (arr 1) of the 20-min mean pulses. The standard deviation is 4.6 dB. (b) The timeseries of arrival-time for each arr 1 peak [dB level shown in (a)] with mean removed. The standard deviation is 2.4 ms. (c) A scatterplot of arrival delay-time anomaly [(in (b)] versus peak level [in (a)] shows no correlation. (d) Seven estimates of the spectrum of the data [in (b)] are shown. The parameter p is the signal subspace dimension used in each eigenvector method spectral estimation. Peaks near one and two cycles/d, and other frequencies, can be seen in all spectra, although with low confidence level (not shown).

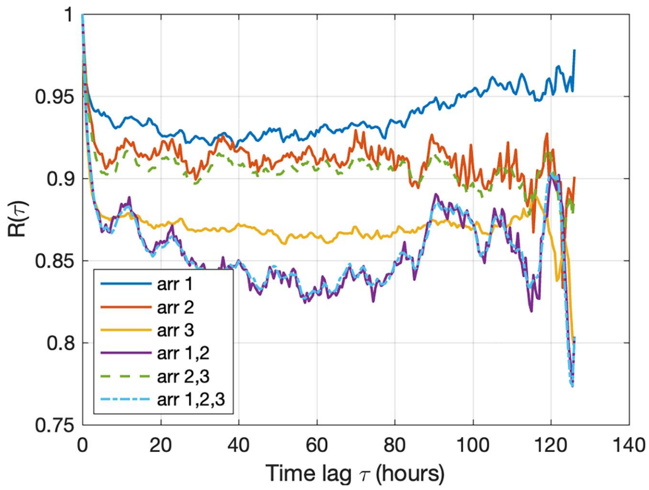

FIG. 10. The normalized correlation functions $R(\tau)$ for time series $\Phi(t_f,t)$ are shown for the 20-min window-mean pulses for the three arrival sections displayed in Figs. 2 and 6. The first strong arrival (arr 1, fast time 7.22–7.27 s) has the highest correlation over time, with arr 2 being the next highest. Correlation is lower for arr 3. The [arr 1 arr 2] time window of 7.22–7.35 s has a low correlation, similar to the result for a wider window ([arr 1 arr 2 arr 3], 7.22–7.45 s). The curves for arr 2 and [arr2 arr3] are similar.

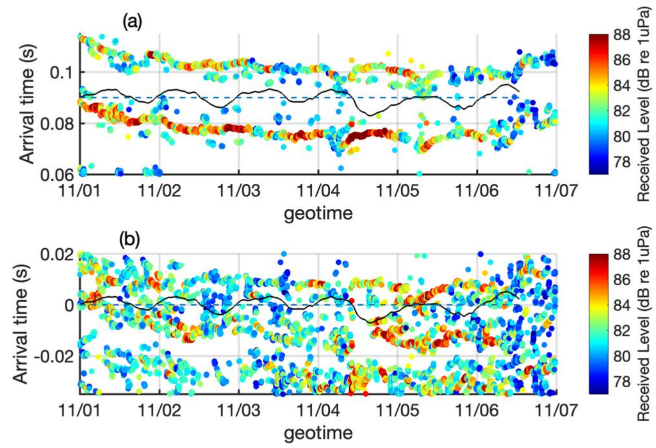

FIG. 11. (a) Matched-filtered pulse arrivals at Rx3 of Fig. 4(b) are replotted to show two persistent arrivals in more detail. The black line indicates the time series of depth-averaged sound-speed measured at W1, near the receiver, with maximum value 1528.8 and minimum 1520.8 m/s. The effect of the deep diurnal wave can be seen. (b) A different subset of Rx3 matched-filtered pulse arrivals from Fig. 4(b) is plotted.

eigenvalues to include in the signal subspace for spectral computation. Spectral peaks appear in tidal bands of one and two cycles per day in a few spectral estimates. Spectrum computations for the peak-level fluctuation time series do not show any tidal peaks. The analysis does not support the hypothesis that the observed tide-linked motions have a strong acoustic signature.

The pulse-to-pulse correlation analysis used for the 20-min windows was also applied to the window-mean pulses. Figure 10 shows the results. The correlation coefficient drops significantly below the high 20-min values of Fig. 8, falling below 0.94 for the first arrival (arr 1) after a few hours, and falling below 0.87 for the third (fluctuating) arrival (arr 3). The correlation for a longer pulse section containing arr 1 and arr 2 (fast time 7.22–7.35 s) is lower than it is for arr 1 or 2, implying that the individual arrivals have independent fluctuations, so that the wave form changes shape over time. The curves also reflect the fact that arr 1 and arr 2 carry virtually all of the energy for mean pulses computed in 20-min segments (arr 1, 2 and arr 1, 2, 3 curves almost identical).

D. Rx3 arrivals

The Rx3 arrivals are a blend of isolated steady arrivals, closely spaced arrivals that are difficult to separate and track, and intermittently detected arrivals that probably appear at times of low noise. The automated detector analysis method does not allow the effects of noise to be examined, nor arrival patterns to be examined with complete detail. Nonetheless, some aspects of arrival variation can be examined. Figure 11(a) shows some arrivals in detail. The isolated steady arrival at 0.08 s reduced time shows a 15-dB variation (the color scale is saturated), while the next arrival at 0.1 s show less variation. On November 4–6, the 0.08 s arrival also shows a diurnal oscillation in arrival time, somewhat anti-correlated with the plotted depth-averaged sound speed. This is the most notable example of a diurnal tidal oscillation that we have found in these data. These time variations exceed those caused by sensor motions (see next paragraph). The delay of arrivals under conditions of lower sound speed is an intuitive effect that is readily understandable for high-angle paths that are governed more by boundaries than by refraction. However, the effect is not seen every day for this arrival, and is not present for other arrivals. The 0.08 s arrival amplitude shows hints of a diurnal cycle, three high-intensity peaks November 3–5, although these are spaced apart less than 24 h. Figure 11(b) shows many untrackable arrivals with timing and amplitude variations at many time scales, including subtidal.

The pressure sensor records from Tx and Rx3 showed that Tx had a limited horizontal displacement, oscillating by about 1 m (mean –0.0476 m; SD 0.3862) and that Rx3 horizontal displacement was also limited to about 1 m. These showed oscillations consistent with diurnal tides as well as a large single displacement event in the second half of November 6. The measurements of the oscillation of a mooring with respect to the other, when accounting for the sound speed at 90 m of depth recorded by W1, are consistent with variations of the measured pulse travel time of maximum on 6 November of 3.5 ms, with SD of less than 0.2 ms. The large 6 November displacement is excluded from acoustic analysis. The low displacements at the other times contribute insignificant error to our analysis and interpretation.

The matched-filtered Rx3 phone 4 waveforms show strong temporal variations not seen in the Rx2 dataset, although the full scope of variations is not fully captured in the automated Rx3 arrival data (Figs. 4 and 11). Two full matched-filter waveforms, midstream in the automated analysis, are shown in Fig. 12. These are waveforms spaced 12 h

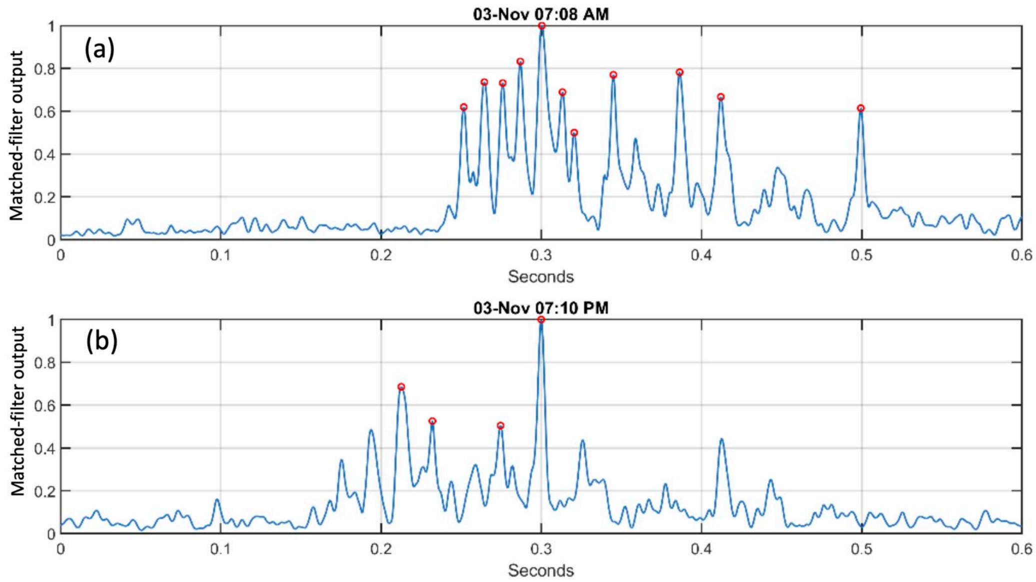

FIG. 12. Matched-filter Rx3 output at high tide (top) and at low tide (bottom). Red circles indicate the flagged and analyzed multipath arrivals (11 arrivals at 07:08 AM, 4 at 07:10 PM). In other words, the red-circle flagged peaks appear in Figs. 4 and 11. Time zero is set 0.3 s before the highest peak in these two plots only.

in time. At the time of the first waveform (about 7 AM), the ocean has high depth-averaged sound speed (deepened lower isopycnals), the other has low average sound speed (see sound speed in Fig. 3 and average sound-speed curves in Fig. 11). The early selection shows 11–13 peaks, and the highest peak is not prominent above the others. The later selection has one tall peak surrounded by six or seven other peaks. The implication is that steeper upslope propagation in the final 20 km of the Tx to Rx3 path is strongly impacted by the water column, with such impact not seen in the Tx to Rx2 path.

E. Simulated arrivals

The BELLHOP computational model (Porter, 2011) was used to simulate 3D propagation over the experiment paths. A parallelized version (bellhopcxx) from the University of California San Diego was used (https://github.com/A-New-BellHope/bellhopcuda). The purpose was to understand the propagation geometry of the stable arrival pattern. BELLHOP simulates underwater sound propagation by computing rays and using beam propagation theory to build sound fields around those rays. Here, the model is used to find rays that contribute sound at the receivers, and then to compute the temporal impulse response consistent with those rays. The model produces various output parameters that are useful for understanding the nature of the simulated sound. Two water-column sound-speed field conditions were considered. One is a uniform (range-independent) sound-speed profile throughout the area, and the second is a 3D-variable sound-speed snapshot from a data-assimilating numerical model of the area developed for this project (Oddo *et al.*, 2023).

Figure 13 shows a simulated pulse arrival at 85-m depth at Rx2, and parameters of the rays that contribute to the simulated pulse. Seabed properties used here were acoustic wave speed 1600 m/s, shear wave speed 0 m/s, density 1800 kg/m^3, and p-wave attenuation 0.8 dB per wavelength (type 1 seabed, here). The 3D variable sound-speed field

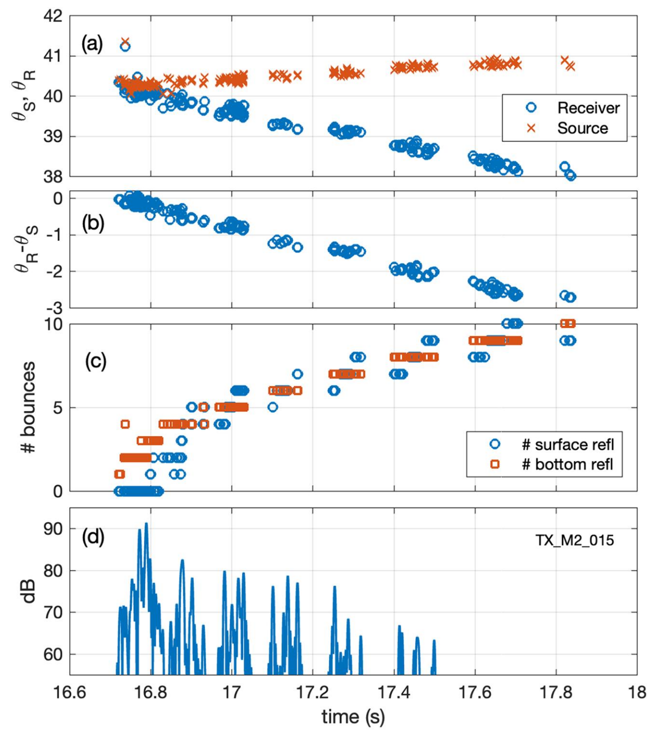

FIG. 13. (a) The headings at the source and the receiver of rays received at Rx2 in a BELLHOP3D model run for November 8 model conditions, bottom type 1. Heading in degrees is plotted using math convention, so that 0° is east and 45° is northeast. The sound arrives first going in the direction 40°, then arrives traveling gradually more easterly. The early arrivals are nearly straight-line, while the later rays are deflected to the right. (b) Ray deflections computed using the points in (a) are plotted. (c) The number of surface reflection and bottom reflections is plotted for each ray. (d) The simulated broadband synthesized waveform is plotted, also shown in Fig. 5.

from the 0200 UTC November 7 snapshot of the data-assimilating model put together for this area was used (Oddo *et al.*, 2023). This snapshot was late in the experiment and incorporates more experimental observations than earlier snapshots. The initial arrival rays are close to straight-line in plan view, whereas the rays that follow are deflected to the right looking toward the receiver, with deflection increasing with time up to 3° at 1 s of delay. The number of surface reflections of these rays increases from 0 to 10 with time, while the number of bottom reflections increases from 1 to 10. The maximum excursion of eigenrays to the left side of the straight-line path (looking from source to receiver) is 140 m (not plotted). The simulated pulse arrival bears some resemblance to the measured pulse, with both plotted in Fig. 5. Seven distinct groups of multipath arrivals are seen in the simulated pulse [Figs. 5 and 13(a)–13(d)]. Each group of arrivals shares a common number of bottom reflections [Fig. 3(c)], with three different numbers of surface reflections in each group. Bottom reflections range from 5 to 10 for the six delayed groups. The ray groups are also distinguished by vertical declination angle (not plotted). The first group has angles between 0° and 10° from the horizontal (upward or downward), consistent with rays not intersecting the seabed or grazing the seabed. The second group (five bottom reflections) has ray-angle absolute values between 11° and 14°. The third group has values of 15°–16°, and these angles continue upward to 24° for the seventh group. Upslope conversion causes declination to increase with each reflection. The multiple groups of dispersed arrivals are similar to those observed for a 10-km upslope path off the South New England shelf (DeCourcy *et al.*, 2022).

Inspection of Fig. 5 shows that the arrivals are split into two types: a single long set of arrivals, then four groups of horizontally deflected arrivals each with a fixed number of implied bottom reflections (from 5 to 8). These arrive at times 0.02–0.6 s in the model, and times 0.1–0.6 s in the data. Some time misalignment may be caused by errors in the bathymetric database. The initial extended set of arrivals, for few bottom bounces, has a different character in the simulation and the data, which may be caused by inaccuracies in the model sound speed field or the model bathymetry. The main peak arrivals, with two bottom reflections, are modeled to have intensity near that seen in the data, but the later arrivals with more bottom reflections are too strong in the simulations. This implies that the additional reflections are not attenuated enough in the model. Reducing the seabed acoustic wave speed, changing to an elastic medium seabed type to divert energy to shear waves, and increasing attenuation would each serve to decrease the seabed reflection coefficient. Considering the option of a seabed inversion, it is apparent that signal attenuation is not proportional to the number of seabed reflections for the later, steeper arrivals, despite the restricted range of ray grazing angles (10°–25°), and that full 3D propagation physics with a variable seabed would be needed to fully utilize the data. For example, using duration and amplitude to estimate energy in each group of arrivals, and accounting for noise, the relative energies for the 5, 6, 7, and 8 seabed reflection groups are 0, –4.7, – 9.1, and –10.1 dB. The similarity of the energy in the final two received groups is notably inconsistent with a simple reflection model.

Simulations of sound emitted from Tx and received at Rx3 were performed for three seabed types. The seabed sound-speed of 1600 m/s (seabed type 1) used for the Rx2 simulation was again used. Two additional sound speeds were also used: 1720 m/s and 1520 m, which yield high and low bottom reflection in BELLHOP, respectively. Figure 14 shows the results. For this sound path, the received sound is deflected to the left up to 4° as it propagates in the type 1 simulation. All sound reflects off the seabed a least four times in the simulation.

The type 1 seabed yields sound that is attenuated more than 15 dB from its peak value at times outside of a 0.08 s main arrival window. The data show strong arrivals spread over more than 0.2 s, so this is a little inconsistent. The more reflective seabed shows strong arrivals about 0.2 s after the main early peak, better matching the data in this respect, yet inconsistent with the data because the simulated energetic sound window (above –15 dB re peak) extends 0.6 s longer than in the data. Although we attempt to mitigate the effect of varying SNR by looking here at the strongest 15 dB of signal, low SNR and processing restrictions may mask some sound in the data.

The time-dependence of the Rx3 multipaths illustrated in Fig. 12 was investigated with a time series of 2D BELLHOP simulations using the 4D-variable ocean model

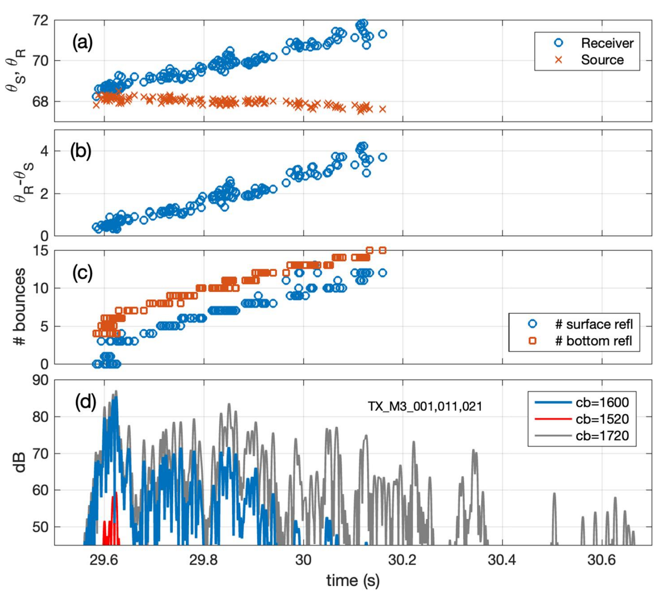

FIG. 14. Similar to Fig. 13, showing simulated sound at Rx3 from Tx. (a) The headings at the source and the receiver of contributing rays are shown for the bottom-type 1 model. Units are degrees counterclockwise from east. The initial arrivals are nearly straight-line, while the later rays are deflected to the left. (b) Ray deflections computed using the points in (a) are plotted. (c) The number of surface reflection and bottom reflections is plotted for each ray. (d) The simulated broadband synthesized waveform is plotted for the bottom-type 1 simulation (1600 m/s bottom sound speed), and for two other simulations with the listed seabed sound speeds.

https://doi.org/10.1121/10.0043949

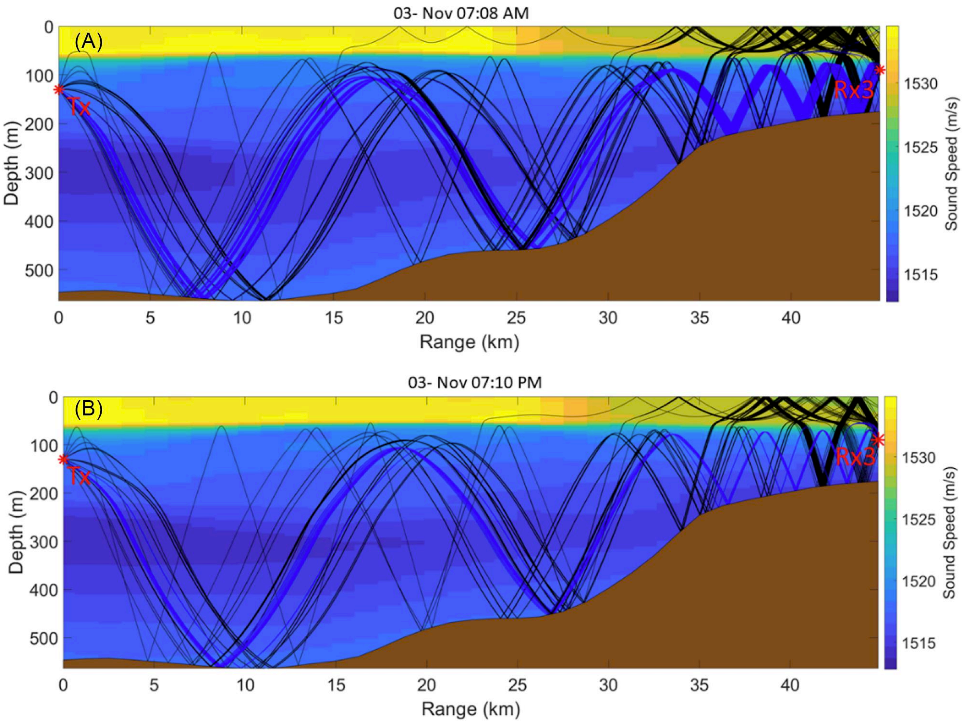

FIG. 15. Modeled ray paths between Tx and Rx3 during the early morning (A) at 07:08 AM and during the late afternoon (B) at 07:10 PM overlaid on the modeled sound speed field. Rays in blue interact only with the bottom.

fields. The eigenrays at the times of the Fig. 12 waveforms are shown in Fig. 15.

The 7 AM regimen returns a higher number of ray interactions with both the surface and the bottom, when compared with the 7 PM regimen. The process of the sound penetrating into the surface duct (mixed layer) is very sensitive to model details, for example, the tilt of the upper surface of the transition layer (Colosi and Rudnick, 2020). This tilt is also quantifiable as variable surface layer depth, which can occur with IT displacements, as observed in our records but likely not accurately represented in the models because of sensitivities to grid spacing, bathymetry, and stratification (Ponte and Cornuelle, 2013; Zhang *et al.*, 2014; Duda *et al.*, 2016). Nonetheless, some aspects of the IT signals in the model are consistent with observations. The sound-speed at the depth of the receiver (90 m) fluctuates with semidiurnal frequency on the Tx end of the Tx-Rx3 path (not illustrated). Semidiurnal variability is also seen in the middle of the path, although 90-m depth sound speed is lower here than at Tx. Moving toward Rx3, the sound speed fluctuation become mainly diurnal. Thus, the modeling agrees with the observations (Poulain *et al.*, 2023), who found that the diurnal K1 signal in the vertical displacement of isopycnals is significantly enhanced on the Maltese Bank.

IV. DISCUSSION

The data show notable sound properties. Our main findings are as follows:

1. The 25-km path sound at Rx2 is remarkably steady. It is extremely coherent over 20-minute periods, with R generally well above 0.92 (Figs. 6–8), and very coherent over 6 days, with R above 0.85 (Fig. 10).
2. The diurnal oscillation that dominates the sound-speed anomalies in the area does not cause dominant diurnal sound-field fluctuations. A few cycles of diurnal sound travel-time fluctuation are seen in the longer 45-km path to Rx3 [Fig. 11(a)].
3. Multipath fading is one cause of temporal decorrelation, but steady multipaths overwhelm the effects of intermittent fades to maintain coherency of the overall waveform at Rx2 (Fig. 6 shows multipath arrival time series with correlation values in Fig. 7).
4. The simulated pulses do not match the data very well. This may be caused by a lack of 2D high-resolution bathymetric data, such as can be obtained with multibeam survey sonar. However, the Rx2 arrivals validate the model suggestion that sound arrives in multipath groups that each have a common bottom-reflection count, with each group increasingly horizontally deflected with reflection count, with deflection up to 3° (Fig. 5).

Expanding on point (1), the full-waveform correlation coefficients greater than 0.97 for 20 min (Fig. 7) are notable. It is important to note that many underwater acoustics studies showing rapid sound decorrelation have been done at sites chosen for their active dynamic features. The purpose of those was to identify and quantify strong episodic effects on the sound (e.g., Badiey *et al.*, 2005; Chiu *et al.*, 2004; Duda *et al.*, 2004, 2012; Sperry *et al.*, 2003). This study did not target a site of pronounced water-column variations, and it shows that steady sound can exist, at times, for seabed-interacting sound in a Mediterranean Sea slope environment. This work provides a valuable benchmark for long-duration coherence in upslope propagation conditions.

The signal stability is consistent with weak scattering. For example, in the limit of zero fluctuation, signals will never decorrelate. On the other hand, the intensity variations for the multipath (ray path) arr 1 shown in Fig. 9(a) are strong, with scintillation index (SI) of 0.97, far greater than the weak scattering limit of about 0.3, with SI defined as intensity (amplitude squared) variance divided by the square of mean intensity. SI near 1 implies saturation, interference of many microrays with uncorrelated fluctuations. For rays that are water-column refracted, and not strongly affected by boundary reflection, fluctuation behavior has been examined in many studies in terms of the strength parameter (Φ), which is close to the RMS phase fluctuation in most situations, and a diffraction parameter Λ, which is related to intensity variation (Lynch *et al.*, 2006; Colosi, 2015 and 2016; Esswein and Flatté, 1980). In particular, Colosi (2015) lists estimates of these parameters for many experiments and compares observed versus predicted sound fluctuation behavior. These parameters are computed using models for internal waves, and can be used to delineate a weak-scattering regimen and stronger-scatter saturated fluctuation regimens where rays split into groups of interfering microrays. In partial saturation, microray fluctuations are correlated, while in full saturation microrays behave independently. Multipath arr 1 is largely refracted, with three or fewer boundary reflections, so we make a brief examination of the Λ-Φ theory. Previously, Sliwka and Fabbri (2023) presented a Λ-Φ analysis of MREP20 sound-speed data and sound data recorded at Rx2. The sound was from a 3-kHz source 13 km to the NE of Rx2. The along-path depth varied by about 10% and was not strictly upslope. They found conditions along rays on that path to be consistent with weak scattering bordering on partial saturation ($\Lambda\Phi^2 \sim 2$), and verified this Λ-Φ regimen for supertidal-frequency sound fluctuations (tidal-band fluctuations removed). They show Φ of 7–10 radians and Λ of 0.02–0.07. Here, using $\Phi = 2\pi f \sigma_t$, $f = 750$ Hz and RMS time perturbation $\sigma_t = 2.4$ ms for arr 1 [Fig. 9(b)], we have $\Phi = 11.3$, which is close to the value for the 13-km path. Sliwka and Fabbri employ an expression appropriate for weak scattering, $\Lambda = 4\mathrm{SI}\Phi^{-2}$, which is not appropriate for arr 1 because unity SI implies the saturation regimen where SI is independent of details of the medium that are quantified in terms of the parameters. Nonetheless, using that expression gives us $\Lambda = 0.03$ for arr 1. Because $\mathrm{SI} \sim 1$, Λ may indeed be much higher, beyond where SI is proportional to it. For $\Phi = 11.3$, Λ would need to exceed 0.1 for full saturation (see Λ-Φ diagrams in the references). Regardless of our diffraction parameter uncertainty and despite the possibility that boundary reflection effects not covered in the Λ-Φ theory may be contributing to intensity fluctuations, our lengthy correlation times for the entire waveform and for arr 1, and low Φ for arr 1, suggest that sound-speed perturbations along the separate ray paths, and any reflection geometry perturbations, are weak and uncorrelated between paths, and have no trends, resulting in the overall arrival pattern being steady for 5 days.

Our Rx2-received signals showed a high coherence within 20-min time windows, with correlation $R > 0.93$ up to a delay of 20 min. Moreover, R remained above 0.75 over the 6 days of transmission. Previously, LFM signals with center frequencies of 450, 1200, and 3550 Hz transmitted in Mediterranean Sea showed much lower coherence even at shorter ranges (Yang, 2006). Coherence values were also lower in the ASIAEX experiment (Duda *et al.*, 2004), with values dropping below 0.6 within about 6 min of delay and reaching 0.7 between 50 and 200 s of delay throughout the length of the transmissions.

Finding (2) follows directly from the fact that the sound is passing through the oscillating deep layers at large grazing angle. The time spent in the layer of perturbations caused by the deep oscillation is minimal, so the travel time anomalies are low. Also, intensity fluctuations generally result from encounters with changes in the sound speed gradient and second derivative normal to the path of the sound, so perturbations to gradients and second derivatives at turning points dominate this process for vertical cycling rays (Duda and Bowlin, 1994; Colosi, 2016; DeFilippis *et al.*, 2023). The findings agree with theory that internal-wave based sound fluctuations are created at water-column turning points (Colosi, 2016) because the rays have zero, one, or two turning points. Scattering effects during the more numerous reflections from the rough surface for the later (steeper) rays cause the later signals to fluctuate more, but these carry only a small energy fraction.

Finding (3), that multipath fading reduces coherence in an identifiable way, is illustrated in Figs. 6 and 7. Figure 6 shows such fading for arrival 1 at analyzed geotime 2, followed by the onset of a new arrival (columns 3 and 4, lowest panels). This event causes the lowest 20-min correlation value of the 12 curves plotted in Fig. 7(a), for the 12 acoustic records of Fig. 6, and the lowest full waveform correlation [Fig. 7(b)].

Finding (4) stems from the fact that the bathymetry and the water column are not precisely known. Despite the unknowns, a few points can be made about the patterns. Our Rx2 arrival patterns and the modeled patterns have similarities with patterns in DeCourcy *et al.* (2022). They did not observe leading arrivals with intensity higher than the dispersed groups, which we did observe for our 25-km path. On the other hand, their modeling produced the intense leading arrival pattern (leading arrivals have fewer seabed reflections). DeCourcy *et al.* (2022) attribute the modeled intense arrivals to surface ducting along at least a portion of the path, which is difficult to model without accurate mixed-layer depth. Our modeling shows that the early bottom-reflecting arrivals may have incident angles with the seabed of 10°–12°, low angles that may increase their energy in a manner that is beyond the scope of this paper to determine.

V. CONCLUSION

Previous studies conducted using oceanographic data from our research campaign indicate that the Malta Plateau is characterized by ocean dynamics at the diurnal and semi-diurnal frequencies. The diurnal K1 tidal oscillation is modulated fortnightly with amplitudes of 15–25 m at 160 m of depth. Its greatest amplitude is near the seafloor, and there is only weak oscillation of the surface mixed layer base. This oscillation gets stronger moving from the deeper water onto the shelf (Poulain *et al.*, 2023). Semidiurnal oscillations were also measured, but they were much smaller. A subsequent numerical modeling study (Oddo *et al.*, 2023) evidenced that the K1 oscillations behave as Kelvin-like bottom trapped waves propagating southward, generated by the interaction of the barotropic tidal flow with the steep bathymetry. Despite all these dynamical internal ocean features, the sound field of the area remained stable during our sound transmission experiment. While several cycles of diurnal sound fluctuations were measured along the longer Rx3 path, diurnal tides had little impact on temporal coherence of which we have quantified in detail on the shorter Rx2 path. Moreover, our study demonstrated that upslope sound transmissions along two paths in the Malta Plateau are very coherent over our observation period of 6 days. Signals received in our experiment showed a high coherence over 20-min periods. The correlation coefficient was higher than 0.93 up to a delay of 20 min, and remained above 0.75 over the 6 days of transmission. These are lower bounds for coherence because processing steps to remove out-of-band noise were not done.

Of note is that acoustic simulations did not match the acoustic observations. This is not surprising given the uncertainties in the water column sound speed and the bathymetry for this strongly bottom-interacting sound. The quantities and locations of seabed interactions of the multipath arrivals are potentially knowable with better information. At this time, the data support the hypothesis of a heterogeneous seabed in the area because the number of seabed reflections does not strongly track with signal strength of the arrival groups, which have distinct numbers of seabed reflections.

ACKNOWLEDGMENTS

This work was made possible by the MREP20 participants. CMRE led the cruise preparations and data collection, supported by NATO Allied Command Transformation. WHOI components were supported by U.S. Office of Naval Research (ONR) Grant No. N00014-17-1–2624, ONR Grant No. N00014-22-1–2547, and NATO-CMRE Award No. 42000790. Nico Llanos and James Kuo of WHOI operated the Tx and Rx2 systems and endured COVID-19 international travel quarantines. Peter Koski of WHOI prepared the sound source. The work of other members of the WHOI Mooring Operations Support and Mooring Fabrication groups is acknowledged, along with the work of numerous CMRE professionals. The efforts of the captain and crew of *Alliance* are appreciated.

AUTHOR DECLARATIONS

Conflict of Interest

The authors have no conflicts to disclose.

DATA AVAILABILITY

Data are archived at Harvard Dataverse. Posted files include processed W1 data, matched-filtered Rx2 arrivals, Rx3 picked peak arrivals, plus Bellhop input parameter, ray, and arrival files. Some data and software supporting this research are restricted by government policies. Data and software are available in the CMRE servers, with access restricted only to governmental institutions of NATO member nations and are not accessible to the public or research community. Should the need arise, the dataset and software could be disclosed upon viable request via the establishment of a non-disclosure agreement. A formal request for the disclosure of the data can be addressed to the NATO CMRE contact point via the official website: https://www.cmre.nato.int/.

Astraldi, M., Balopoulos, S., Candela, J., Font, J., Gacic, M., Gasparini, G. P., Manca, B., Theocharis, A., and Tintoré, J. (**1999**). "The role of straits and channels in understanding the characteristics of Mediterranean circulation," Prog. Oceanogr. **44**(1), 65–108.

Astraldi, M., Gasparini, G. P., Sparnocchia, S., Moretti, M., and Sansone, E. (**1996**). "The characteristics of the water masses and the water transport in the Sicily Strait at long time scales," Bull. Institut. Oceanogr. Monaco, special **17**, 95–115.

Astraldi, M., Gasparini, G. P., Vetrano, A., and Vignudelli, S. (**2002**). "Hydrographic characteristics and interannual variability of water masses in the central Mediterranean: A sensitivity test for long-term changes in the Mediterranean Sea," Deep Sea Res. I **49**, 661–680.

Badiey, M., Katsnelson, B. G., Lynch, J. F., Pereselkov, S., and Siegmann, W. L. (**2005**). "Measurement and modeling of three-dimensional sound intensity variations due to shallow-water internal waves," J. Acoust. Soc. Am. **117**(2), 613–625.

Béranger, K., Mortier, L., Gasparini, G. P., Gervasio, L., Astraldi, M., and Crépon, M. (**2004**). "The dynamics of the Sicily Strait: A comprehensive study from observations and models," Deep Sea Res. II **51**, 411–440.

Chiu, C.-S., Ramp, S. R., Miller, C. W., Lynch, J. F., Duda, T. F., and Tang, T.-Y. (**2004**). "Acoustic intensity fluctuations induced by South China Sea internal tides and solitons," IEEE J. Oceanic Eng. **29**, 1249–1263.

Colosi, J. A. (**2015**). "A reformulation of the Λ-Φ diagram for the prediction of ocean acoustic fluctuation regimes," J. Acoust. Soc. Am. **137**, 2485–2494.

Colosi, J. A. (**2016**). *Sound Propagation through the Stochastic Ocean* (Cambridge University Press, New York).

Colosi, J. A., and Rudnick, D. L. (**2020**). "Observations of upper ocean sound-speed structures in the North Pacific and their effects on long-range acoustic propagation at low and mid-frequencies," J. Acoust. Soc. Am. **148**(4), 2040–2060.

Cosoli, S., Drago, A., Ciraolo, G., and Capodici, F. (**2015**). "Tidal currents in the Malta-Sicily Channel from high-frequency radar observations," Cont. Shelf Res. **109**, 10–23.

Colosi, J. A., Van Uffelen, L. J., Cornuelle, B. D., Dzieciuch, M. A., Worcester, P. F., Dushaw, B. D., and Ramp, S. R. (**2013**). "Observations of sound-speed fluctuations in the western Philippine Sea in the spring of 2009," J. Acoust. Soc. Am. **134**(4), 3185–3200.

DeCourcy, B. J., Lin, Y.-T., Zhang, W. G., Ozanich, E. R., Kukshtel, N., Siderius, M., Gawarkiewicz, G., and Forsyth, J. (**2022**). "Real-time joint ocean acoustics and circulation modeling in the 2021 New England Shelf Break Acoustics experiment (L)," J. Acoust. Soc. Am. **152**, 2859–2862.

DeFilippis, J. P., Cornuelle, B. D., Lucas, A. J., Hodgkiss, W. S., Lenain, L., Kuperman, W. A., and Alford, M. H. (**2023**). "Observations and simulations of caustic formation due to oceanographic fine structure," J. Acoust. Soc. Am. **154**, 1372–1388.

Duda, T. F., and Bowlin, J. B. (**1994**). "Ray-acoustic caustic formation and timing effects from ocean sound-speed relative curvature," J. Acoust. Soc. Am. **96**, 1033–1046.

Duda, T. F., Collis, J. M., Lin, Y.-T., Newhall, A. E., Lynch, J. F., and DeFerrari, H. A. (**2012**). "Horizontal coherence of low-frequency fixed-path sound in a continental shelf region with internal-wave activity," J. Acoust. Soc. Am. **131**, 1782–1797.

Duda, T. F., Lynch, J. F., Newhall, A. E., Wu, L., and Chiu, C.-S. (**2004**). "Fluctuation of 400 Hz sound intensity in the 2001 ASIAEX South China Sea experiment," IEEE J. Oceanic Eng. **29**, 1264–1279.

Duda, T. F., Zhang, W. G., Helfrich, K. R., Lin, Y.-T., and Newhall, A. E. (**2016**). "Modeling internal solitary wave development at the head of a submarine canyon," in *8th International Symposium on Stratified Flows*, San Diego, CA.

Esswein, R., and Flatté, S. M. (**1980**). "Calculation of the strength and diffraction parameters in oceanic sound transmission," J. Acoust. Soc. Am. **67**, 1523–1531.

Flatté, S. M., Dashen, R., Munk, W. M., Watson, K. M., and Zachariasen, F. (**1979**). *Sound Transmission through a Fluctu ating Ocean* (Cambridge University Press, Cambridge)

Grancini, G. F., and Michelato, A. (**1987**). "Current structure and variability in the Strait of Sicily and adjacent area," Ann. Geophys., Ser. B **5**(1), 76–88.

Johnson, J. J., Lin, Y.-T., Newhall, A. E., Gawarkiewicz, G. G., Knobles, D. P., Chaytor, J. D., and Hodgkiss, W. S. (**2023**). "Acoustic ducting by shelf water streamers at the New England shelfbreak," JASA Express Lett. **3**, 086001.

Lermusiaux, P. F. J. (**1999**). "Estimation and study of mesoscale variability in the Strait of Sicily," Dyn. Atmos. Oceans **29**, 255–303.

Lermusiaux, P. F. J., and Robinson, A. R. (**2001**). "Features of dominant mesoscale variability, circulation patterns and dynamics in the Strait of Sicily," Deep Sea Res. I **48**(9), 1953–1997.

Lozano, C. J., and Candela, J. (**1995**). "The M2 tide in the Mediterranean Sea: Dynamic analysis and data assimilation," Oceanol. Acta **18**(4), 419–441.

Lynch, J. F., Colosi, J. A., Gawarkiewicz, G., Duda, T. F., Pierce, A. D., Badiey, M., Katsnelson, B. G., Miller, J. H., Siegmann, W., Chiu, C-.S., and Newhall, A. (**2006**). "Consideration of fine-scale coastal oceanography and 3-D acoustics effects for the ESME sound exposure model," IEEE J. Oceanic Eng. **31**, 33–48.

Marple, S. L. (**1987**). *Digital Spectral Analysis* (Prentice-Hall, Englewood Cliffs, NJ).

Merrifield, M. A., Holloway, P. E., and Johnston, T. S. (**2001**). "The generation of internal tides at the Hawaiian Ridge," Geophys. Res. Lett. **28**, 559–562, https://doi.org/10.1029/2000GL011749.

Mignerey, P. C., and Orr, M. H. (**2004**). "Observations of matched-field autocorrelation time in the South China Sea," IEEE J. Oceanic Eng. **29**, 1280–1291.

Millot, C. (**1987**). "Circulation in the Western Mediterranean Sea," Oceanol. Acta **10**, 143–149.

Morozov, E. (**2006**). "Internal tides: Global field of internal tides and mixing caused by internal tides," in *Waves in Geophysical Fluids: Tsunamis, Rogue Waves, Internal Waves and Internal Tides*, Springer, Vienna, pp. 271–332.

Munk, W., and Wunsch, C. (**1998**). "Abyssal recipes: II. Energetics of tidal and wind mixing," Deep Sea Res. I **45**, 1977–2010.

Nansen, F. (**1902**). "The oceanography of the North polar basin," in *The Norwegian North Polar Expedition, 1893–1896, Scientific Results* (Longmans, Green, and Co., London).

Oddo, P., Poulain, P.-M., Falchetti, S., Storto, A., and Zappa, G. (**2023**). "Internal tides in the central Mediterranean Sea: Observational evidence and numerical studies," Ocean Dyn. **73**, 145–163.

Petterson, O. (**1907**). "Strumstudien vid Östersjöns portar" ("Current studies at the gates of the Baltic Sea"), Inst. Mar. Res. Lysekil Set. Biol. Rep. **3**, 13–37.

Ponte, A. L., and Cornuelle, B. D. (**2013**). "Coastal numerical modelling of tides: Sensitivity to domain size and remotely generated internal tide," Ocean Modell. **62**, 17–26.

Porter, M. B. (**2011**). *The BELLHOP Manual and User's Guide: Preliminary Draft* (Heat, Light, and Sound Research, La Jolla, CA).

Poulain, P.-M., Menna, M., and Gerin, R. (**2018**). "Mapping Mediterranean tidal currents with surface drifters," Deep Sea Res. I **138**, 22–33.

Poulain, P.-M., Oddo, P., Pennucci, G., Lewis, C., Sliwka, J., Duda, T. F., and Drago, A. (**2023**). "Observations of internal tidal dynamics Southwest of Malta in the central Mediterranean Sea," Cont. Shelf Res. **254**, 104922.

Robertson, R., and Hartlipp, P. S. (**2014**). "Tidal effects on acoustic propagation off eastern Australia," in *Proceedings of Internoise*.

Sliwka, J., and Fabbri, T. (**2023**). "Comparing predicted and observed strength and diffraction parameters for characterizing transmissions through a fluctuating water body," *10th Convention of the European Acoustics Association*, Turin, Italy, pp. 6119–6126.

Sperry, B. J., Lynch, J. F., Gawarkiewicz, G., Chiu, C.-S., and Newhall, A. (**2003**). "Characteristics of acoustic propagation to the eastern vertical line array receiver during the summer 1996 New England shelfbreak PRIMER experiment," IEEE J. Oceanic Eng. **28**, 729–749.

St. Laurent, L., and Garrett, C. (**2002**). "The role of internal tides in mixing the deep ocean," J. Phys. Oceanogr. **32**, 2882–2899.

St. Laurent, L., Stringer, S., Garrett, C., and Perrault-Joncas, D. (**2003**). "The generation of internal tides at abrupt topography," Deep Sea Res. I **50**, 987–1003.

Tiemann, C. O., Worcester, P. F., and Cornuelle, B. D. (**2001**). "Acoustic scattering by internal solitary waves in the Strait of Gibraltar," J. Acoust. Soc. Am. **109**(1), 143–154.

Tsimplis, M. N., Proctor, R., and Flather, R. A. (**1995**). "A two-dimensional tidal model for the Mediterranean Sea," J. Geophys. Res. **100**(C8), 16223–16239, https://doi.org/10.1029/95JC01671.

Wunsch, C. (**1975**). "Internal tides in the ocean," Rev. Geophys. **13**, 167–182, https://doi.org/10.1029/RG013i001p00167.

Yang, T. C. (**2006**). "Measurements of temporal coherence of sound transmissions through shallow water," J. Acoust. Soc. Am. **120**(5), 2595–2614.

Zhang, W. G., Duda, T. F., and Udovydchenkov, I. A. (**2014**). "Modeling and analysis of internal-tide generation and beamlike onshore propagation in the vicinity of shelfbreak canyons," J. Phys. Oceanogr. **44**, 834–849.